Dynamical characterization of transport barriers in nontwist Hamiltonian systems

M. Mugnaine,[1] A. C. Mathias,[2] M. S. Santos,[1] A. M. Batista,[1,3] J. D. Szezech, Jr.,[1,3,*] and R. L. Viana[2]
[1]*Graduate Program in Sciences, State University of Ponta Grossa, Ponta Grossa, Paraná, Brazil*
[2]*Department of Physics, Federal University of Paraná, Curitiba, Paraná, Brazil*
[3]*Department of Mathematics and Statistics, State University of Ponta Grossa, Ponta Grossa, Paraná, Brazil*

(Received 21 November 2017; published 22 January 2018)

The turnstile provides us a useful tool to describe the flux in twist Hamiltonian systems. Thus, its determination allows us to find the areas where the trajectories flux through barriers. We show that the mechanism of the turnstile can increase the flux in nontwist Hamiltonian systems. A model which captures the essence of these systems is the standard nontwist map, introduced by del Castillo-Negrete and Morrison. For selected parameters of this map, we show that chaotic trajectories entering in resonances zones can be explained by turnstiles formed by a set of homoclinic points. We argue that for nontwist systems, if the heteroclinic points are sufficiently close, they can connect twin-islands chains. This provides us a scenario where the trajectories can cross the resonance zones and increase the flux. For these cases the escape basin boundaries are nontrivial, which demands the use of an appropriate characterization. We applied the uncertainty exponent and the entropies of the escape basin boundary in order to quantify the degree of unpredictability of the asymptotic trajectories.

DOI: 10.1103/PhysRevE.97.012214

I. INTRODUCTION

One of the outstanding issues in the theory of Hamiltonian dynamical systems is the study of transport, which aims to characterize the motion of groups of trajectories from one region of the phase space to another [1]. There is a plethora of physical applications of transport in Hamiltonian systems, such as celestial mechanics [2], chemical reactions [3], condensed matter [4], plasma confinement [5], particle accelerators [6], fluid advection [7,8], and mixing in granular media [9].

A description of transport is particularly difficult in nonintegrable Hamiltonian systems, due to the fact that there are periodic, quasiperiodic, and chaotic orbits mixed together in a nontrivial fashion [10]. In a seminal paper, MacKay *et al.* reported that the dynamical mechanism underlying transport in nonintegrable Hamiltonian systems is the partial barriers formed by joining the gaps in invariant Cantor sets, also known as cantori [11]. For area-preserving twist maps, the Kolmogorov-Arnold-Moser (KAM) theorem warrants the existence of invariant tori with sufficiently irrational rotation numbers, as long as the perturbation is weak enough [12]. An increase in the perturbation strength can destroy those irrational tori, leaving there cantori as remnants of the destroyed tori [13]. The cantori are the most robust transport barriers in any region of the phase space.

Another dynamical feature that affects the transport in nonintegrable Hamiltonian system is the presence of partial barriers bounding resonance zones. As is well known, the Poincaré-Birkhoff theorem states that a rational torus will be destroyed by a perturbation, leaving behind a set of elliptic and hyperbolic points (centers and saddles, respectively) [14]. A resonance zone consists of periodic islands surrounding the centers, whose boundaries are formed from the stable and unstable manifolds of the saddles [1]. The set formed by two such contiguous lobes is named a turnstile, since it works like a revolving door, permitting transport across the corresponding barrier.

While most of the known results on transport assume that the Hamiltonian system displays the twist condition, it is an open question whether or not the above description would apply to nontwist systems as well. In Ref. [1] Meiss considers this one of the two key questions to be answered by future work on this subject. On the other hand, nontwist systems appear in various problems of physical interest, like toroidal devices with reversed magnetic shear [15], traveling waves in geophysical zonal flows [16,17], laser-plasma coupling [18], the advection of a passive scalar by an incompressible shear fluid flow [19], and the $\mathbf{E} \times \mathbf{B}$ drift motion of charged particles in a magnetic field [17,20]. For systems like these it is important to characterize the presence of internal transport barrier in order to explain the cessation or reduction of transport.

In this work, we explore numerical diagnostics of transport in chaotic area-preserving nontwist systems, in such a way as to explain some features of the transport across internal partial transport barriers. An example of the nontwist system, which has been intensively studied in the past two decades, is the standard nontwist map. We take this map as a paradigm for the dynamical behavior of nontwist systems in general. For this nontwist map we combine the numerical computation of the transmissivity across the internal transport barrier with the recently introduced concept of basin entropy to identify the basin boundary of the escape regions related to transport across the barrier [21].

We show that the turnstiles are indeed responsible for increasing transport fluxes across transport barriers in nontwist systems, just in the way that they do for twist ones. We also characterize the unpredictability of the asymptotic state of

*jdsjunior@uepg.br

the system, analyzing how the transmissivity of the barrier is affected by the invariant manifold structure responsible for the formation of turnstiles.

The paper is organized as follows: in Sec. II we introduce the nontwist standard map and some of its basic properties. The transmissivity of the internal transport barriers in this system is discussed in Sec. III. The concepts of basin entropy and basin boundary entropy are introduced in Sec. IV, with respect to the escape basins related to the barrier transmissivity. Section V is devoted to the interpretation of the numerical results in terms of the turnstile mechanism, and how it can explain the increasing of the transport flux due to trajectories crossing the resonance zones. Our conclusions are found in the last section.

II. STANDARD NONTWIST MAP

A canonical mapping with the general form

$$\begin{aligned} J_{n+1} &= J_{n+1}(J_n,\theta_n), \\ \theta_{n+1} &= \theta_{n+1}(J_n,\theta_n) \end{aligned} \tag{1}$$

is said to satisfy the so-called twist condition if

$$\left|\frac{\partial\theta_{n+1}(\theta_n,J_n)}{\partial J_n}\right| > 0, \tag{2}$$

for every value of (J_n,θ_n). If this condition fails to be obeyed somewhere in the phase space, the map is called nontwist.

The standard nontwist map (SNM) was introduced by del Castillo-Negrete and Morrison; it is defined by the expressions [22]

$$\begin{aligned} y_{n+1} &= y_n - b\sin(2\pi x_n), \\ x_{n+1} &= x_n + \omega(y_{n+1}) = x_n + a\left(1-y_{n+1}^2\right) \mod 1, \end{aligned} \tag{3}$$

where $x \in [0,1)$ and $y \in \mathbb{R}$. The parameters a and b are independent and their values are in the range $a \in [0,1)$ and $b \in \mathbb{R}$ [22]. The SNM is an area preserving map and it is described by the Hamiltonian [22]

$$\begin{aligned} H(x,y,n) = H_0(y) + H_1(x,n) &= ay\left(1-\frac{y^2}{3}\right) \\ &- \frac{b}{2\pi}\cos(2\pi x)\sum_{m=-\infty}^{\infty}\delta_{nm}, \end{aligned} \tag{4}$$

where $\delta_{nm} = \delta(n-m)$.

If $b = 0$, the SNM represents an integrable system and the trajectory for an initial condition lies straight on lines that circle around the x domain [23]. The function $\omega(y)$ in (3) can be identified by the winding number, and its derivative is the shear. The latter does not change sign, provided $\omega(y)$ is either monotonically increasing or decreasing, thus satisfying the twist condition (2). For the map in Eq. (3) $J_n = y_n$ and $\theta_{n+1} = x_{n+1}$, and the twist condition (2) is violated, since

$$\left|\frac{\partial x_{n+1}(x_n,y_n)}{\partial y_n}\right| = |\omega'(y_n)| = 0, \tag{5}$$

for $y_n = 0$ and for (x_n,y_n) along the so-called shearless curve in the phase space, which is the loci where the shear changes sign [24]. The quadratic dependence of ω on y leads to two invariant curves with the same winding number at both sides of the shearless curve. For $b \neq 0$ we observe two island chains structured on each invariant curve, and they are separated by a shearless invariant torus.

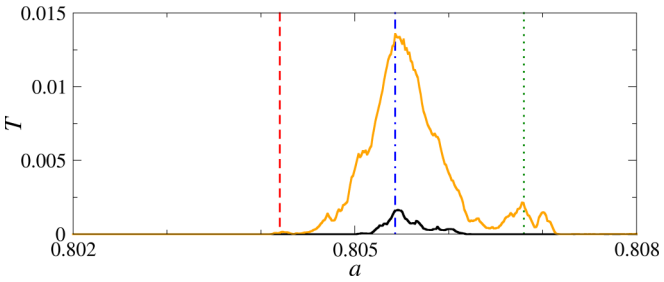

FIG. 1. Transmissivity of the SNM for $b = 0.6$ with the final time $n = 100$ and $n = 400$, represented by the black and the orange (light gray) curves, respectively. The red (blue) dashed (dash-dotted) line indicates an a value that represents low (high) transport in the phase space. We mark a secondary peak at $a = 0.8068$ in dotted green line.

The violation of the twist condition by the SNM has as a consequence diverse bifurcations like periodic orbit collision and separatrix reconnection [23]. The type of bifurcation that rises in the nonlinear dynamics is influenced by the nonmonotonicity inherent in the system [25]. In a chaotic regime, reconnections as rearrangements of level curves, as defined in [26], could not occur, but the "manifold reconnection" is possible [25]. The manifold reconnection is the rearrangements of the set of stable and unstable manifold originated in hyperbolic points from a situation of intracrossing (mutual crossing absent) to an intercrossing situation (frequent mutual crossing) [25,27]. The reconnection occurs between manifolds from different chains of islands and the outcome is an observable influence in the transport through the phase space [25].

The island chains bordering the shearless curve are the transport barriers, in the sense that chaotic orbits in both sides of it do not mix. Even after the manifold reconnection, for a weak perturbation, the transport is hindered if the shearless curve still exists. Only after that curve is destroyed is there transport across the internal partial barrier.

III. TRANSPORT ACROSS THE INTERNAL PARTIAL BARRIER

We assume the existence of a transport barrier between two chains of islands embedded in a large chaotic orbit contained in the interval $-0.8 < y < 0.8$, for appropriate values of the parameters a and b. One direct measure of the transport across the barrier is the transmissivity T, defined as the fraction of the number of orbits that cross the barrier over the total number of orbits in a given time [27]. To investigate the influence of the barrier in the transport we place $N = 10^6$ initial conditions on the line $y = -0.8$. Then, we iterate them for two different times, $n = 100$ and $n = 400$, counting the number of trajectories that cross the line $y = 0.8$.

In Fig. 1 we see the dependence of the transport on the parameter a for $b = 0.6$. There is a primary peak (blue dash-dotted line) in the transmissivity for $a = 0.8054$ and $n = 100$ (black curve), indicating a high transport level through the phase space. Our goal is to investigate the difference between the high (blue dash-dotted line) and the low (red

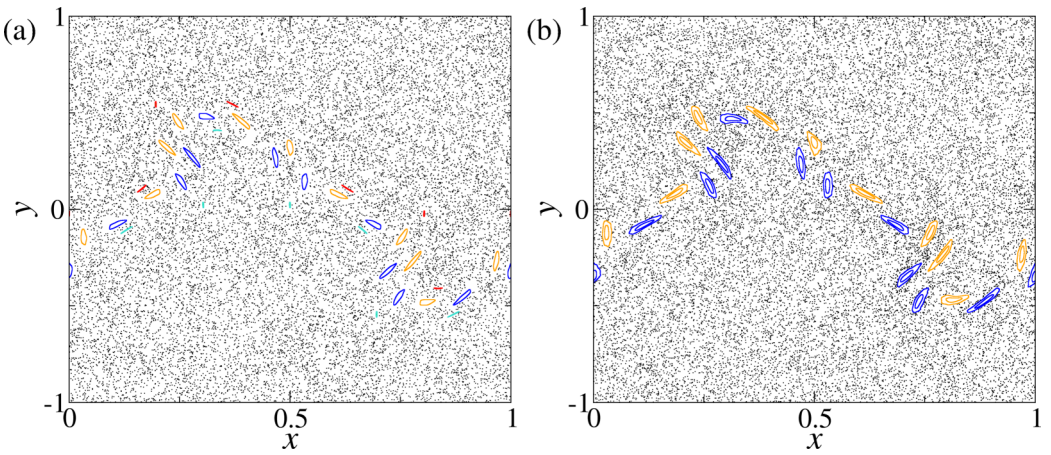

FIG. 2. Phase spaces of the SNM for $b = 0.6$ and (a) $a = 0.8042$ (low transport) and (b) $a = 0.80543$ (high transport). The orange (light gray) and blue (dark gray) curves represent the upper and lower period-11 island chain remnants.

dashed line) transport and the mechanism that led the system to a high transmissivity regime. The low and high transport cases are represented by the parameters $(a,b) = (0.8042,0.6)$ and $(a,b) = (0.805\,43,0.6)$, respectively. The respective phase spaces are shown in Fig. 2.

A secondary peak of transport appears for $n = 400$, represented by the orange (light gray) curve, about $(a,b) = (0.8068,0.6)$ indicating the other value of high transmissivity. However, the higher value of the primary peak over the secondary peak indicates that the transport of the first case occurs on a shorter time scale. There is not a significative difference between the phase spaces of the low and high transport cases, represented by the red (dashed) and blue (dash-dotted) lines in Fig. 1, respectively.

The global dynamics of the SNM for the large chaotic regions, as shown in Fig. 2, suggests that a typical chaotic trajectory can diffuse either to large positive or negative values of y. If a shearless curve (perfect transport barrier) exists, it is relatively easy to distinguish the initial conditions that tend to large positive or negative y. However, if the shearless curve has broken up, a partial barrier is left therein, making it possible that trajectories cross the barrier.

One useful concept is the escape basin: let the two exits A and B be the lines $y = 1$ and $y = -1$, and we consider the phase space region $\{[0,1) \times (-1,1)\}$. The escape basin of exit A (respectively B) is the set of initial conditions that generate trajectories that, after some specified time interval τ, cross the line $y = 1$ (respectively $y = -1$). If this time τ is large enough, there can still exist orbits that do not escape, either because they are trapped within small periodic islands or due to a strong stickiness effect. The values $y = \pm 1$ are quite arbitrary but, as long as they are placed far away from the transport barrier, the results are not expected to change.

In Fig. 3 we determine the escape basin for two exits mentioned above. We use a grid of 5000×5000 initial conditions over the phase space region $\{[0,1) \times (-1,1)\}$. If an initial condition originates a trajectory that passes through $y = 1$ or $y = -1$, its position is marked by a blue (dark gray) or green (light gray) pixel, respectively. If the trajectory does not escape until the time limit $n = 400$, we leave a blank point. If there is a perfect transport barrier separating the two chains of islands, we have a well-defined separation between the blue (dark gray) and green (light gray) regions, which is the escape basin boundary [28]. Accordingly, in Fig. 3(a) the escape basin

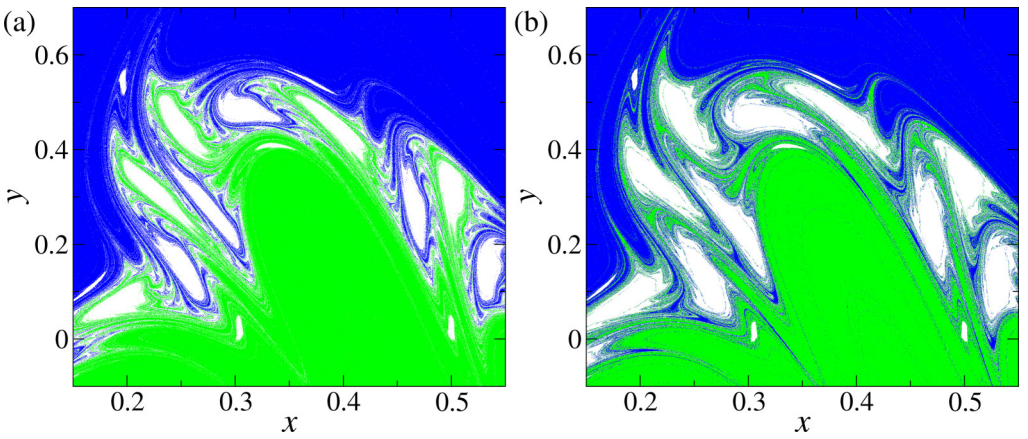

FIG. 3. Escape basins for the SNM for $b = 0.6$ and (a) $a = 0.8042$, (b) $a = 0.805\,43$. The blue (dark gray) and green (light gray) basins represent the set of initial conditions that escape through the exit $y = 1.0$ and $y = -1.0$, respectively, within $n = 400$ map iterates.

boundary is well defined and there is no mixing between the green (light gray) and the blue (dark gray) regions. In this case, we can say that the escape basin boundary is the transport barrier itself.

For the high transport case in Fig. 3(b), we see the two regions overlapping and forming incursive fingers [28]. Thus, before the breakup of the transport barrier, there were initial conditions that belonged to the blue (dark gray) escape basin; after the barrier breakup, they begin to belong to the green (light gray) escape basin. The extremely convoluted nature of the escape basins and of the corresponding boundaries suggests a fractality that can only be accessed by proper numerical diagnostics, as it will be shown in the next section.

IV. CHARACTERIZATION OF ESCAPE BASINS

The presence of incursive fingers in the near-barrier region of Figs. 3(a) and 3(b), and the corresponding intertwining of the corresponding escape basins, is typical of fractal structures in nonlinear dynamics. These fractal structures are basically formed by the meandering of the invariant stable and unstable manifolds of unstable periodic orbits in the near-barrier region. One example is the cantorus formed by the remnants of invariant tori with a self-similar gap structure akin of the Cantor set. In this section, we characterize numerically the fractal behavior of the escape basins and their boundaries using appropriate diagnostics.

A. Uncertainty dimension

The concept of uncertainty dimension has been long introduced in the literature of dissipative dynamical system, being a fast and reliable way to estimate the box-counting dimension D of the basin boundary between two basins of attraction. It was rapidly recognized that its usefulness lies beyond the realm of dissipative systems, being applied to basins of escape in open Hamiltonian systems, for example. We can thus refer, in general, to "basins of behavior," when referring to a set of initial conditions in phase space which leads to the same behavior, either the convergence of a given attractor, an escape through a given exit, or some similar concept.

Let the basin belong to a two-dimensional phase space, and let $N(\delta)$ be the minimum number of squares of side δ necessary to cover the basin boundary. Then its box-counting dimension is $D = \lim_{\delta \to 0} \ln N(\delta)/\ln(1/\delta)$, such that $N(\delta)$ scales as δ^{-D} for small enough δ [29].

The uncertainty dimension, on the other hand, quantifies the final-state uncertainty of the points belonging to two or more basins. In the terms of escape basins used in this work, we can denote A and B the escape basins colored in blue (dark gray) and green (light gray), respectively, as shown in Fig. 3. We randomly pick up a large number of initial conditions (x_0, y_0) in a region of phase space (near the transport barrier), then iterate the SNM until the corresponding trajectories reaches the corresponding exit ($y = 1.0$ for points belonging to A and $y = -1.0$ for those in B).

We performed the calculation of the uncertainty exponent using 2×10^4 initial conditions randomly distributed over the interval $0 \leqslant x_0 < 1$ and $-0.7 < y_0 < 0.7$. For each initial condition (x_0, y_0) we choose $(x_0 \pm \varepsilon, y_0)$ then we iterate until it escapes. If all initial conditions converge to the same escape, we refer to the initial condition as ε certain, otherwise as ε uncertain. The fraction of ε-uncertain points is expected to scale with ε as a power law $f(\varepsilon) \sim \varepsilon^{\alpha}$, where α is the so-called uncertainty exponent. It can be shown that $\alpha = 2 - D$, such that, if the basin boundary is smooth ($D = 1$), then $\alpha = 1$, whereas fractal basin boundaries have $0 < \alpha < 1$ [30].

TABLE I. Escape basin boundary uncertainty dimension for the cases shown in Fig. 2, with $b = 0.6$ and final time evaluated after $n = 400$ iterations of the SNM.

Parameter a	Uncertainty dimension D	Correlation coefficient R
0.8042	1.905 ± 0.003	0.9957
0.80543	1.906 ± 0.002	0.9983
0.8068	1.905 ± 0.003	0.9967

We consider three situations indicated in Fig. 1, for $b = 0.6$ and $a = 0.8042$ (low transmissivity), 0.805 43 (high transmissivity) and 0.8068 (intermediate transmissivity); the respective escape basins are shown in Figs. 4(b)–4(d). The $f(\varepsilon)$ is estimated as the ratio of the number of ε-uncertain by the total number of initial conditions iterated for $n = 400$. Figure 4(a) exhibits the log-log of $f(\varepsilon)$ as a function of ε, where the angular coefficient gives the uncertainty exponent α. By means of α we compute the basin boundary dimension D (Table I). In addition, we included error bars estimated to be the square root of the number of uncertain conditions.

The basin boundary dimension partially answers the question of how unpredictable is the outcome of a given trajectory. The α values are less than 1 for the three situations, indicating the presence of the fractal basin boundary, i.e., there is a final state sensitivity. However, the values are not significantly different from each other. The fractal dimension boundary does not give us an answer about the difference of the transport for each case. This open question could be better explained in terms of basin entropy.

B. Basin entropy

The results obtained from the uncertainty dimension point out that the escape basin boundary is fractal, indicating an uncertainty with respect to the final state. However, if we want to know whether or not one escape basin is more unpredictable than the other, the uncertainty dimension gives no answer. To answer this question, Sanjuán *et al.* have recently introduced the concept of basin entropy [31].

We divide the phase space in N boxes, each of them containing a number N_c of initial conditions which evolve through time towards a given escape. Let a positive integer i denote a box ($i = 1,2,\ldots N$) and j a possible escape ($j = 1,2,\ldots N_A$). For the ith box, the fraction of initial conditions escaping through the jth exit defines a probability p_{ij}, such that the entropy of each box is [21]

$$S_i = -\sum_{j=1}^{N_A} p_{ij} \log_{10}(p_{ij}). \tag{6}$$

In our case there are only $N_A = 2$ escapes, hence the entropy of each box varies from 0, if all the initial conditions inside

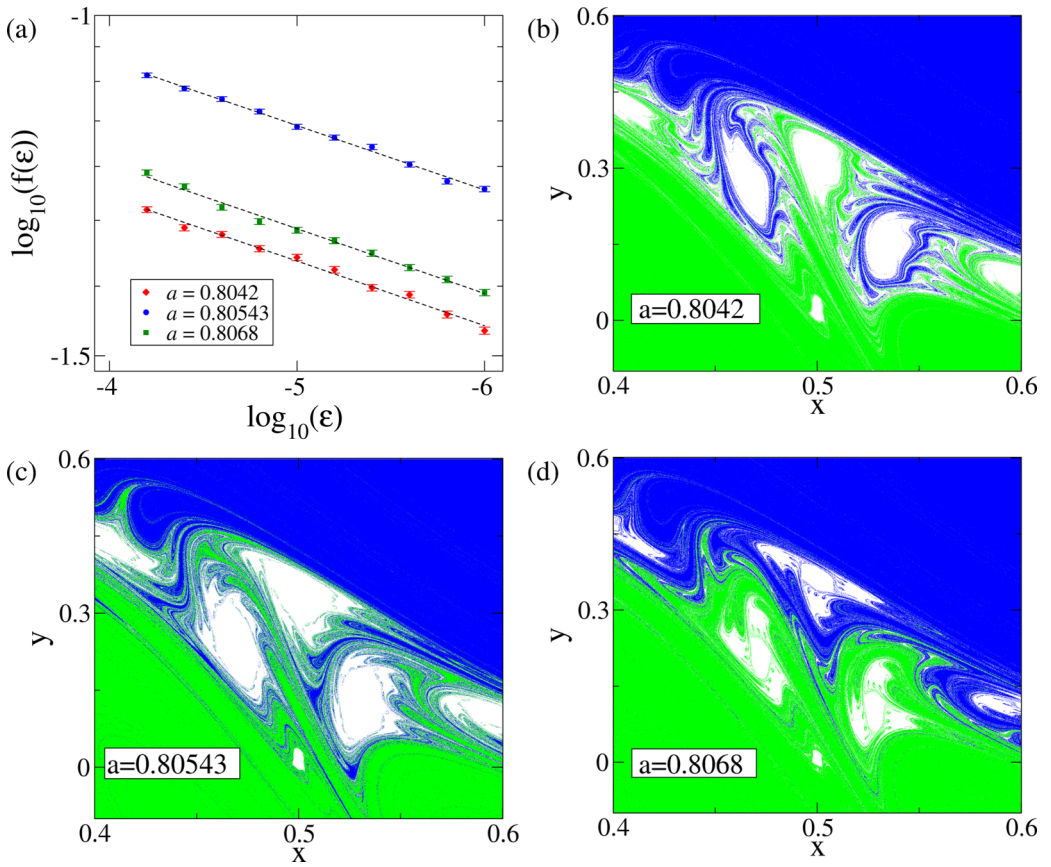

FIG. 4. (a) Log-log plot of the fraction of ε-uncertain points as a function of the scaling box size ε computed for the escape basins of three different values of parameter (b) $a = 0.8042$, (c) $a = 0.805\,43$, and (d) $a = 0.8068$.

a box evolve toward the same exit, and to $\log_{10} 2$, if the initial conditions escape through the two exits with the same probability. The basin entropy is obtained from the average value of the box entropies,

$$S_b = \frac{S}{N} = \frac{1}{N}\sum_{i=1}^{N} S_i. \tag{7}$$

If, out of the N total number of boxes, N_b boxes lie on the basin boundary, we define the boundary basin entropy as $S_{bb} = S/N_b$. The difference between S_b and S_{bb} is that the latter is normalized by the number of boxes intercepting pieces of the basin boundary, whereas S_b considers the total number of boxes.

In principle, for higher values of N and N_c, the value of the basin entropy is more accurate. However, in numerical simulations one has to seek a compromise between statistical convergence and computational time. Accordingly, we have divided the phase space region $-1 < y < 1$ and $0 \leqslant x < 1$ into $N = 2 \times 10^6$ boxes. Within each box, we consider $5^2 = 25$ initial conditions over a grid with spacing $\epsilon = 1 \times 10^{-3}$, and we compute the basin entropy.

We plot in Fig. 5 the basin entropy (S_b) and the boundary basin entropy (S_{bb}) as a function of the parameter a with the same interval as specified in Fig. 1. The main peak of the transmissivity nearly coincides with the maximum value of the basin entropy, at $a = 0.805\,43$. The second largest peak in transmissivity, for $a = 0.8068$, coincides with the secondary peak of the basin entropy. The small peak of T at $a = 0.8042$ is also a peak of S_b.

Moreover, from Fig. 5 we also see that the basin boundary entropy is related to the complexity of the escape basin boundary, since the value of S_{bb} is zero for no transmissivity at all, suggesting a smooth escape basin boundary, which turns out to be the shearless curve. As the basin entropy increases we also see a jump of the basin boundary entropy to a value near 10^{-3} which stays approximately constant in the interval of a values yielding high transmissivity. This indicates that the escape basin boundary is complex when the shearless curve has broken and its remnants make for a partial transport

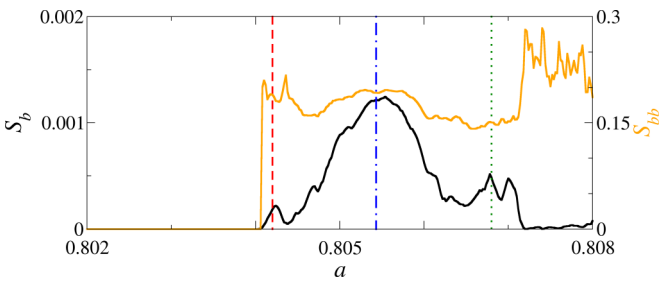

FIG. 5. Comparison of S_b and S_{bb} for different values of the parameter a. The red dashed line represents the low transmissivity, the blue dash-dotted line is the primary peak of transport, and the green dotted line is the secondary peak of transport.

barrier. Indeed, we found that the box-counting dimension of the boundary is fractal for the three cases considered, all of them corresponding to the region of high transmissivity.

It has been proposed that, if $S_{bb} > \ln 2$, then the basin boundary is fractal. This is a sufficient but not necessary criterion for fractality, though, since some fractal basins do not fulfill this condition. This has been observed, for example, in escape basins related to problems in plasma physics, as the $\mathbf{E} \times \mathbf{B}$ drift motion of charged particles in magnetized plasmas [32] and the field line structure in a tokamak with ergodic magnetic limiter [33]. In our case, likewise we have only two exits ($N_A = 2$), the basin boundary entropy is lower than $\ln 2$, and the corresponding dimension is found to be fractal. According to Ref. [31] this criterion would be easily achieved with more than two exits.

The region of no transmissivity for larger a values is curious since, while the basin entropy is practically zero, the basin boundary entropy is not. Since no transmissivity means that a transport barrier has been formed, a nonzero (actually higher) value of S_{bb} suggests that the boundary is fractal. Hence we conclude that the shearless curve has turned into a barrier with very complicated shape, probably a fractal curve, but which divides the phase space into escape basins as before.

V. TURNSTILES

In this section, we describe how apparently similar phase spaces shown in Figs. 2(a) and 2(b) present huge differences in their transmissivity values in Fig. 1. One of the key points to understand those differences is to try to determine the location where the leaky trajectories follow to increase or decrease the transmissivity. For area preserving maps, the Poincaré-Birkoff theorem states that for each fixed stable elliptic point there is a corresponding fixed unstable hyperbolic point. These unstable points generate a tangle of unstable and stable manifolds. The configuration of the tangle interferes in the leak of the trajectories in the phase space. In Refs. [34,35], the location of trajectories that cross barriers can be explained determining the turnstiles and lobes.

However, how does the turnstile mechanism act in the nontwist systems and its transport properties? The existence of twin island chains is a signature of nontwist systems, in this case this providing us a transition for a scenario of intracrossing to intercrossing [27]. The turnstile mechanism is also affected by this transition and has a crucial role in the increase of the transmissivity through the phase space.

Let $\mathbf{O^L}$ ($\mathbf{O^U}$) denote a hyperbolic fixed point of the lower (upper) island chain and its stable and unstable manifolds are represented by W_s^L (W_s^U) and W_u^L (W_u^U), respectively. The points of intersection between W_s^L (W_s^U) and W_u^L (W_u^U) are called homoclinic points of the lower (upper) chain. In particular, we selected one point P from the homoclinic points; we called it principal intersection point (PIP) and name it $\mathbf{P^L}$ ($\mathbf{P^U}$) for the lower (upper) island chain [36,37]. The union of the segments $W_s^L(O,P)$ and $W_u^L(P,O)$ creates upper and lower boundaries of regions in the phase space. The regions delimited by those boundaries form the turnstiles. A trajectory that leaves (or enters) a resonance of a specific island must pass through one of these turnstiles.

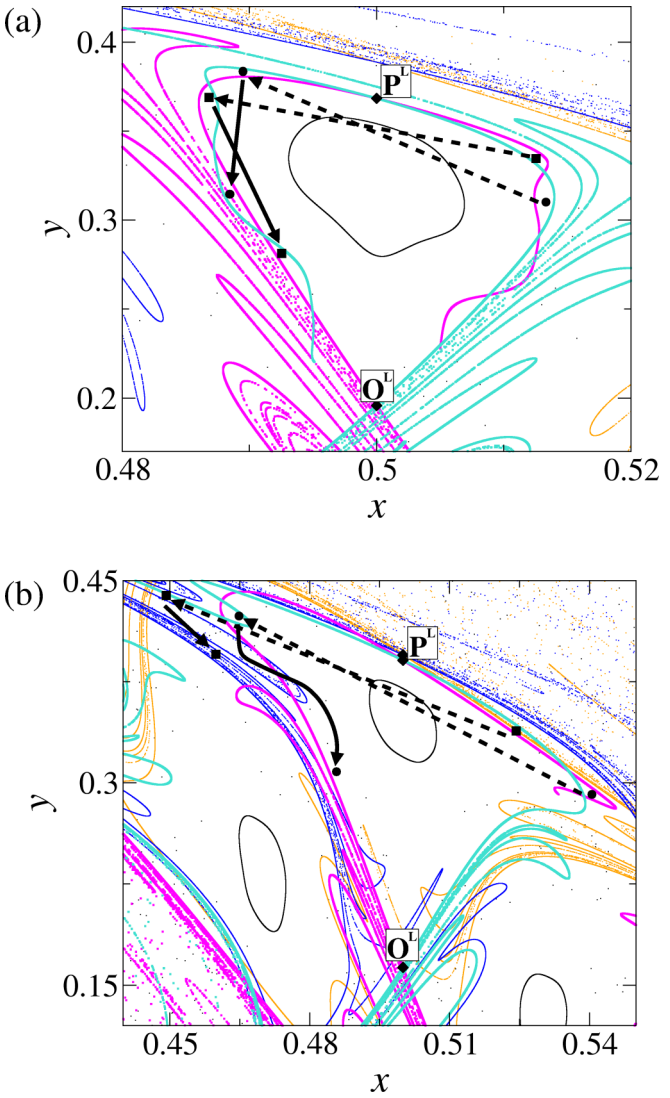

FIG. 6. First and second iterate for the initial conditions (ICs) belonging in the lobe regions for (a) $a = 0.8042$ and (b) $a = 0.805\,43$. Circles and squares indicate the iterates from different ICs. The first (second) iterate is represented by the dashed (solid) line. $\mathbf{O^L}$ ($\mathbf{P^L}$) indicates the hyperbolic (PIP) point of the lower chain.

In Fig. 6(a) we illustrate the turnstile for two trajectories marked by the black arrows near the point $\mathbf{P^L}$. The lower island chain manifolds, W_s^L and W_u^L, are represented by the magenta (thick dark gray) and cyan (thick light gray) lines, respectively. The upper island chain manifolds, W_s^U and W_u^U, are represented by the orange (thin light gray) and blue (thin dark gray) lines, respectively. The trajectory starting from the black square (circle) is outside (inside) the resonance zone; after being iterated two times we observe the trajectory entering (leaving) the resonance zone. In both cases (entering and leaving) the trajectory remains in the lower island chain tangled by the manifolds W_s^L and W_u^L. We attribute this case of intracrossing as due to the homoclinic tangle of the manifolds of the island chains.

In Fig. 6(b) we adopt a similar procedure of the previous case from Fig. 6(a). However, the trajectories from the lower island chain start to follow the W_u^U, represented by the blue

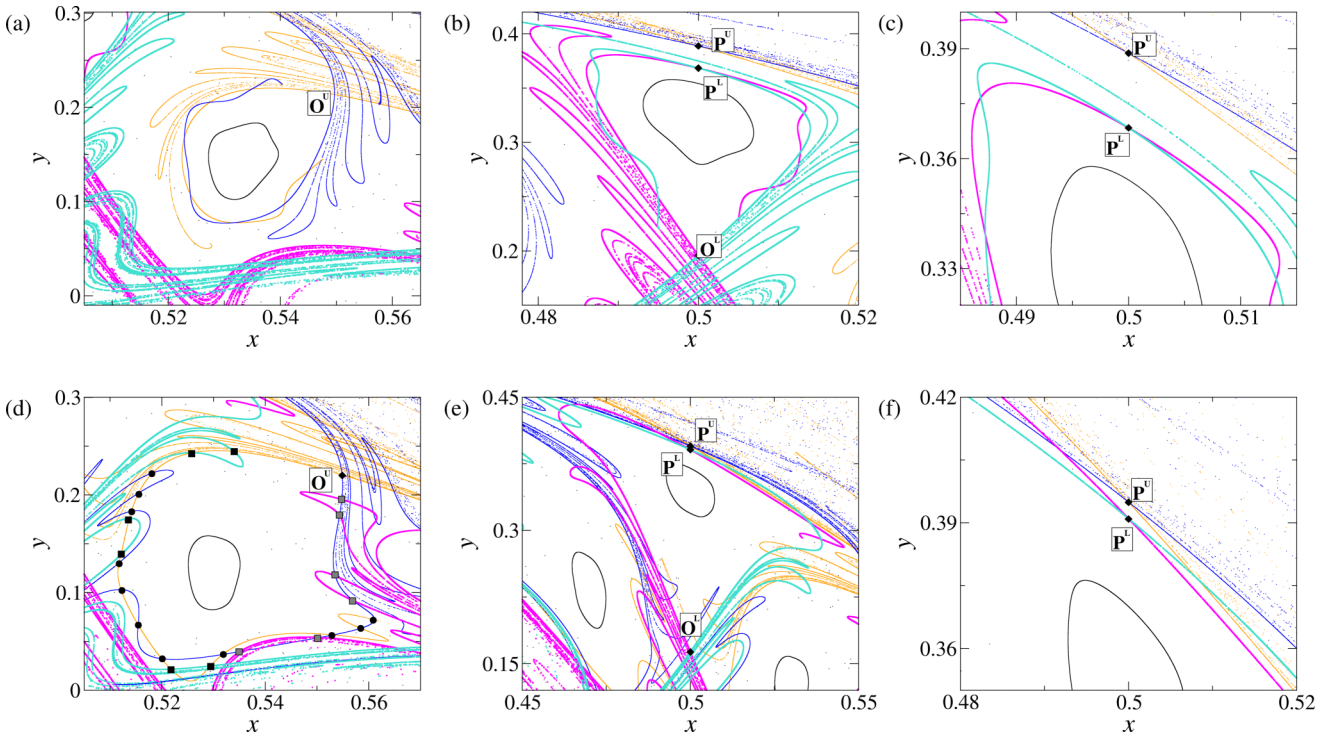

FIG. 7. Principal intersection points (PIPs) for both cases: high ($a = 0.8042$) and low ($a = 0.805\,43$) transport. $\mathbf{O^L}$ ($\mathbf{O^U}$) indicates the hyperbolic point and $\mathbf{P^L}$ ($\mathbf{P^U}$) indicates the PIP from the lower (upper) chain. Full circles represent the PIPs from the intracrossing, while full and hatched squares represented the PIPs from the intercrossing.

(dark gray) line, of the upper island chain after two iterates. This switch of the trajectories between the lower and upper island chain represents a modification of the homoclinic turnstile scenario. Instead, the turnstile describes regions where the trajectories enter or leave a specific island; here it is a case where these trajectories effectively cross the island chains in the phase space. This case represents the intercrossing because there is a heteroclinic tangle between stable and unstable manifolds of the upper and lower island chains.

The mechanism underlying the transition from intracrossing to intercrossing is illustrated in Fig. 7. The circles represent homoclinic points and the black (gray) square represent the heteroclinic points obtained from the crossings between W_s^U and W_u^L (W_u^U and W_s^L). If in the case of Fig. 7(a) we have only homoclinic points, in Fig. 7(d) we observe the simultaneous coexistence of homoclinic and heteroclinic points. Another quantitative characterization of this transition is observed in Figs. 7(b) and 7(e), and for their respective magnifications, Figs. 7(c) and 7(f). In the intracrossing the PIPs $\mathbf{P^U}$ and $\mathbf{P^L}$ have an appreciable distance between each other. On the other hand, the $\mathbf{P^U}$ and $\mathbf{P^L}$ are much closer to each other for the intercrossing.

In Fig. 8(a) for $a = 0.805\,43$, we show where a set of trajectories with $y = 0.8$ and $x \in [0,1)$ follows until reaches $y = -0.8$, in other words those are the leaky trajectories that cross the phase space and increase the transmissivity

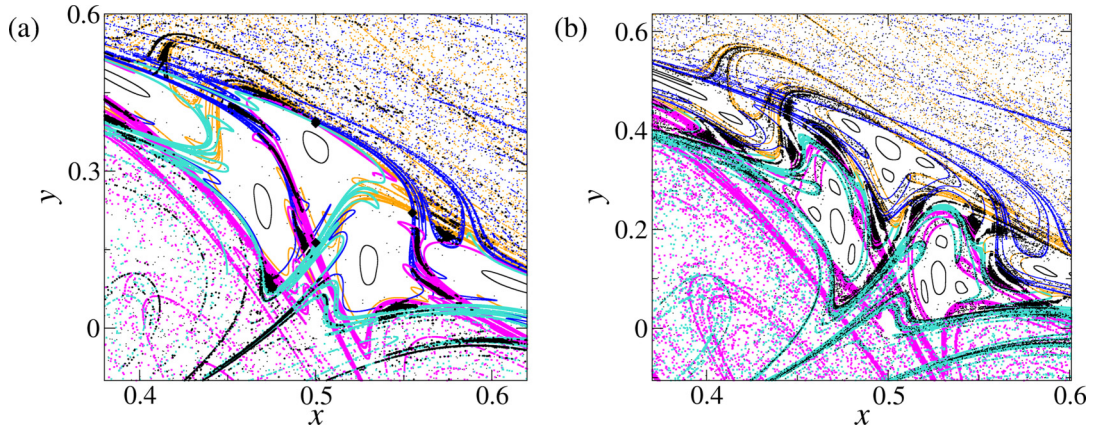

FIG. 8. Flux through the chains of islands for (a) $a = 0.805\,43$ and (b) $a = 0.8068$. The black dots are the trajectories that crossed the phase space for $n = 100$ (a) and $n = 400$ (b).

represented by the blue dash-dotted line in Fig. 1. This leak is also observed in Fig. 8(b) for $a = 0.8068$ (green dotted line in Fig. 1). The crosses between W_s^U and W_u^U of both previous cases form the turnstile (lobe) where the trajectories enter. However, due to the proximity $\mathbf{P^U}$ and $\mathbf{P^L}$ eventually a trajectory reaches the turnstiles formed by W_s^D and W_u^D; in this case the trajectory effectively crosses (leaves) the resonance zone. This way, there is a direct relationship between the proximity of the PIPs and the high transmissivity.

VI. CONCLUSIONS

The formation of transport barriers in nontwist Hamiltonian systems is a typical feature caused by the existence of shearless tori between twin sets of islands, as in the standard nontwist map. We choose parameter values for the latter such that the phase space region is dominated by a large area-filling chaotic orbit, with small remnants of the twin sets of islands. Albeit these islands occupy a relatively small portion of the phase space area available, their effect is strong on the transport properties, since the shearless curve or its remnants form total or partial transport barriers.

The transport flux through the barrier has been characterized numerically by the transmissivity, which is zero if there is a full barrier between the islands. As this barrier is broken, as one of the map parameters is varied, we can separate groups of initial conditions asymptotic to large positive or large negative y values, which we call escape basins. The word escape here must be taken with a grain of salt, because our Hamiltonian system is actually not open. The exit is rather a kind of asymptotic behavior, rather than a proper escape.

In our simulations, we verify that the basins of escape have a fractal boundary when the transmissivity is nonzero, as obtained from an estimate of its box-counting dimension through the computation of uncertainty fraction. In addition, we use the recently developed concept of basin entropy, which measures the unpredictability of the asymptotic state of the system, as defined in the paragraph above. We found that the escape basin entropy varies in the same fashion as the transmissivity does, with a correspondence of the respective peaks. Moreover, the case with the highest basin entropy corresponds to a strongly fractal (almost area-filling) curve.

Another characterization of the transport barrier is provided by the boundary basin entropy. The latter is zero for a regime of no transmissivity at all (for $a \lesssim 0.804$) indicating the presence of a smooth transport barrier, which turns out to be the escape basin boundary as well. In the regime of nonzero transmissivity ($0.804 \lesssim a \lesssim 0.807$) the basin boundary entropy reaches a roughly stationary value, suggesting the presence of a fractal basin boundary. This conclusion is supported by our results for the basin boundary dimension. As for the second region of no transmissivity ($a \gtrsim 0.807$) the basin boundary entropy not only is nonzero, but also its value is higher than in the previous region. We conclude that the transport barrier in this case has a complicated shape, probably a fractal curve.

The numerical characterization that we performed for the transport across the partial barrier is supported by theoretical arguments based on the very nature of the barrier. We concentrated in this work on the role of the PIPs and the turnstiles on the transport properties. When there is some amount of barrier penetration of a given trajectory (i.e., nonzero transmissivity) we have an intercrossing of the trajectories between the twin islands in both sides of the barrier. Hence we can also apply the turnstile hypothesis to the nontwist system, at least when the winding number profile has a local minimum (where the shearless curve lies) and also locally monotonic in both sides of this minimum. The latter condition is naturally verified for the SNM, but we claim that the same scenario would apply to more complicated nontwist systems as well, where we could have this turnstile mechanism acting for each partial transport barrier.

ACKNOWLEDGMENTS

This work was made possible by the partial financial support of CNPq, CAPES, and Fundação Araucária (Brazilian Government agencies). R.L.V. acknowledges valuable discussions with Professor M. A. Sanjuán.

[1] J. D. Meiss, Chaos **25**, 097602 (2015).
[2] W. S. Koon, M. W. Lo, J. E. Marsden, and S. D. Ross, Chaos **10**, 427 (2000).
[3] R. S. MacKay and D. C. Strub, Nonlinearity **27**, 859 (2014).
[4] M. Toller, G. Jacucci, G. DeLorenzi, and C. P. Flynn, Phys. Rev. B **32**, 2082 (1985).
[5] A. H. Boozer, Rev. Mod. Phys. **76**, 1071 (2005).
[6] E. Wilson and E. J. N. Wilson, *An Introduction to Particle Accelerators* (Oxford University Press, New York, 2001).
[7] J. H. E. Cartwright, M. Feingold, and O. Piro, in *Mixing: Chaos and Turbulence*, edited by H. Chaté, E. Villermaux, and J.-M. Chomaz (Springer, Boston, 1999), pp. 307–342.
[8] H. Aref, J. R. Blake, M. Budišić, S. S. S. Cardoso, J. H. E. Cartwright, H. J. H. Clercx, K. El Omari, U. Feudel, R. Golestanian, E. Gouillart, G. F. van Heijst, T. S. Krasnopolskaya, Y. Le Guer, R. S. MacKay, V. V. Meleshko, G. Metcalfe, I. Mezić, A. P. S. de Moura, O. Piro, M. F. M. Speetjens *et al.*, Rev. Mod. Phys. **89**, 025007 (2017).
[9] R. Sturman, S. W. Meier, J. M. Ottino, and S. Wiggins, J. Fluid Mech. **602**, 129 (2008).
[10] R. S. MacKay and J. D. Meiss, *Hamiltonian Dynamical Systems: A Reprint Selection* (Taylor & Francis, London, 1987).
[11] R. S. Mackay, J. D. Meiss, and I. C. Percival, Physica D **13**, 55 (1984).
[12] V. I. Arnold and A. Avez, *Problèmes Ergodiques de la Mécanique Classique*, Monographies Internationales de Mathématiques Modernes (Gauthier-Villars, Paris, 1967).
[13] I. C. Percival, *Nonlinear Dynamics and the Beam-Beam Interaction*, edited by M. Month and J. C. Herrera, AIP Conf. Proc. No. 57 (AIP, New York, 1980), p. 302.
[14] A. Katok and B. Hasselblatt, *Introduction to the Modern Theory of Dynamical Systems*, Encyclopedia of Mathematics and its Applications (Cambridge University Press, Cambridge, England, 1997).
[15] P. J. Morrison, Phys. Plasmas **7**, 2279 (2000).

[16] R. P. Behringer, S. D. Meyers, and H. L. Swinney, Phys. Fluids A **3**, 1243 (1991).
[17] D. del Castillo-Negrete, Phys. Plasmas **7**, 1702 (2000).
[18] A. B. Langdon and B. F. Lasinski, Phys. Rev. Lett. **34**, 934 (1975).
[19] R. T. Pierrehumbert, Phys. Fluids A **3**, 1250 (1991).
[20] W. Horton, H.-B. Park, J.-M. Kwon, D. Strozzi, P. J. Morrison, and D.-I. Choi, Phys. Plasmas **5**, 3910 (1998).
[21] A. Daza, A. Wagemakers, B. Georgeot, D. Guéry-Odelin, and M. A. F. Sanjuán, Sci. Rep. **6**, 31416 (2016).
[22] D. del Castillo-Negrete and P. J. Morrison, Phys. Fluids A **5**, 948 (1993).
[23] D. del Castillo-Negrete, J. M. Greene, and P. J. Morrison, Physica D **91**, 1 (1996).
[24] E. Petrisor, Int. J. Bifurcation Chaos **11**, 497 (2001).
[25] G. Corso and F. B. Rizzato, Phys. Rev. E **58**, 8013 (1998).
[26] J. E. Howard and S. M. Hohs, Phys. Rev. A **29**, 418 (1984).
[27] J. D. Szezech, Jr., I. L. Caldas, S. R. Lopes, R. L. Viana, and P. J. Morrison, Chaos **19**, 043108 (2009).
[28] J. D. Szezech, Jr., I. L. Caldas, S. R. Lopes, P. J. Morrison, and R. L. Viana, Phys. Rev. E **86**, 036206 (2012).
[29] J. Aguirre, R. L. Viana, and M. A. F. Sanjuán, Rev. Mod. Phys. **81**, 333 (2009).
[30] S. W. McDonald, C. Grebogi, E. Ott, and J. A. Yorke, Physica D **17**, 125 (1985).
[31] A. Daza, B. Georgeot, D. Guéry-Odelin, A. Wagemakers, and M. A. F. Sanjuán, Phys. Rev. A **95**, 013629 (2017).
[32] A. C. Mathias, R. L. Viana, T. Kroetz, and I. L. Caldas, Physica A **469**, 681 (2017).
[33] A. C. Mathias, T. Kroetz, I. L. Caldas, and R. L. Viana, Chaos, Solitons Fractals **104**, 588 (2017).
[34] R. S. MacKay, J. D. Meiss, and I. C. Percival, Phys. Rev. Lett. **52**, 697 (1984).
[35] V. Rom-Kedar, A. Leonard, and S. Wiggins, J. Fluid Mech. **214**, 347 (1990).
[36] S. Wiggins, *Global Bifurcations and Chaos: Analytical Methods*, 1st ed., Applied Mathematical Sciences No. 73 (Springer-Verlag, New York, 1988).
[37] H. Fukuda, T. Petrosky, and T. Konishi, Progr. Theor. Exp. Phys. **2016**, 093A01 (2016).